JOURNAL OF GEOPHYSICAL RESEARCH: OCEANS, VOL. 118, 1–15, doi:10.1002/jgrc.20225, 2013

Hydrodynamics of spur and groove formations on a coral reef

Justin S. Rogers,[1] Stephen G. Monismith,[1] Falk Feddersen,[2] and Curt D. Storlazzi[3]

Received 25 September 2012; revised 24 April 2013; accepted 26 April 2013.

[1] Spur and groove (SAG) formations are found on the fore reefs of many coral reefs worldwide. Although these formations are primarily present in wave-dominated environments, their effect on wave-driven hydrodynamics is not well understood. A two-dimensional, depth-averaged, phase-resolving nonlinear Boussinesq model (*funwaveC*) was used to model hydrodynamics on a simplified SAG system. The modeling results show that the SAG formations together with shoaling waves induce a nearshore Lagrangian circulation pattern of counter-rotating circulation cells. The mechanism driving the modeled flow is an alongshore imbalance between the pressure gradient (PG) and nonlinear wave (NLW) terms in the momentum balance. Variations in model parameters suggest the strongest factors affecting circulation include spur-normal waves, increased wave height, weak alongshore currents, increased spur height, and decreased bottom drag. The modeled circulation is consistent with a simple scaling analysis based on the dynamical balance of NLW, PG, and bottom stress terms. Model results indicate that the SAG formations efficiently drive circulation cells when the alongshore SAG wavelength allows for the effects of diffraction to create alongshore differences in wave height without changing the mean wave angle.

Citation: Rogers, J. S., S. G. Monismith, F. Feddersen, and C. D. Storlazzi (2013), Hydrodynamics of spur and groove formations on a coral reef, *J. Geophys. Res. Oceans*, *118*, doi:10.1002/jgrc.20225.

1. Introduction

[2] Coral reefs provide a wide and varied habitat that supports some of the most diverse assemblages of living organisms found anywhere on earth [*Darwin*, 1842]. Reefs are areas of high productivity because they are efficient at trapping nutrients, zooplankton, and possibly phytoplankton from surrounding waters [*Odum and Odum*, 1955; *Yahel et al*., 1998]. The hydrodynamics of coral reefs involve a wide range of scales of fluid motions, but for reef scales of order 100–1000 m, surface wave-driven flows often dominate [e.g., *Monismith*, 2007].

[3] Hydrodynamic processes can influence coral growth in several ways [*Chappell*, 1980]. First, waves and mean flows can suspend and transport sediments. This is important because suspended sediment is generally recognized as an important factor that can negatively affect coral health [*Buddemeier and Hopley*, 1988; *Acevedo et al*., 1989; *Rogers*, 1990; *Fortes*, 2000; *Fabricius*, 2005]. Often, suspended sediment concentrations are highest along the reef flat and are much lower in offshore ocean water [*Ogston et al*., 2004; *Storlazzi et al*., 2004; *Storlazzi and Jaffe*, 2008]. Second, forces imposed by waves can subject corals to high drag forces breaking them, resulting in trimming or reconfiguration of the reef [*Masselink and Hughes*, 2003; *Storlazzi et al*., 2005]. Third, the rates of nutrient uptake on coral reefs [*Atkinson and Bilger*, 1992; *Thomas and Atkinson*, 1997], photosynthetic production and nitrogen fixation by both coral and algae [*Dennison and Barnes*, 1988; *Carpenter et al*., 1991], and particulate capture by coral [*Genin et al*., 2009] increase with increasing water motion.

[4] One of the most prominent features of fore reefs are elevated periodic shore-normal ridges of coral ("spurs") separated by shore-normal patches of sediment ("grooves"), generally located offshore of the surf zone [*Storlazzi et al*., 2003]. These features, termed "spur and groove" (SAG) formations, have been observed in the Pacific Ocean [*Munk and Sargent*, 1954; *Cloud*, 1959; *Kan et al*., 1997; *Storlazzi et al*., 2003; *Field et al*., 2007], the Atlantic Ocean [*Shinn et al*., 1977, 1981], the Indian Ocean [*Weydert*, 1979], the Caribbean Sea [*Goreau*, 1959; *Roberts*, 1974; *Geister*, 1977; *Roberts et al*., 1980; *Blanchon and Jones*, 1995, 1997], the Red Sea [*Sneh and Friedman*, 1980], and other locations worldwide. SAG formations are present on fringing reefs, barrier reefs, and atolls. Typical SAG formations off the fringing reef of southern Moloka'i, Hawai'i, are shown in Figures 1 and 2.

[5] The alongshore shape of the SAG formations varies from smoothly varying rounded spurs [*Storlazzi et al*., 2003], to nearly flat spurs with shallow rectangular channel grooves [*Shinn*, 1963; *Cloud*, 1959], or deeply cut

[1]Environmental Fluid Mechanics Laboratory, Stanford University, Stanford, California, USA.
[2]Scripps Institution of Oceanography, La Jolla, California, USA.
[3]U.S. Geological Survey, Pacific Coastal and Marine Science Center, Santa Cruz, California, USA.

Corresponding author: J. S. Rogers, Environmental Fluid Mechanics Laboratory, Stanford University, 473 Via Ortega, Stanford, CA 94305, USA. (jsrogers@stanford.edu)

2169-9275/13/10.1002/jgrc.20225

Figure 1. Underwater image of a typical SAG formation off southern Moloka'i, Hawai'i. For scale, the height between the sand-floored groove and the top of the coral spurs is approximately 1.5 m, the width of the groove is approximately 2 m. Wave-generated symmetrical ripples cover the sand bed; view is seaward.

rectangular or overhanging channels often called buttresses [*Goreau*, 1959]. The scales of SAG formations vary worldwide, but in general spur height (h_{spr}) is of order 0.5–10 m, SAG alongshore wavelength (λ_{SAG}) is of order 5–150 m, the width of the groove (W_{grv}) is of order 1–100 m, and SAG formations are found in depths (h) from 0 to 30 m below mean sea level [*Munk and Sargent*, 1954; *Roberts*, 1974; *Blanchon and Jones*, 1997; *Storlazzi et al*., 2003].

[6] Although the geometric properties of SAG formations are well documented, analysis of their hydrodynamic function has been limited. On Grand Cayman [*Roberts*, 1974] and Bikini Atoll [*Munk and Sargent*, 1954], SAG formations were shown to be related to incoming wave energy: high incident wave energy areas have well-developed SAG formations, whereas those with low incident wave energy have little to no SAG formations. The SAG formations of southern Moloka'i, Hawai'i, have been well characterized; and incident surface waves appear to exert a primary control on the SAG morphology of the reef [*Storlazzi et al*., 2003, 2004, 2011]. Spurs are oriented orthogonal to the direction of predominant incoming refracted wave crests, and λ_{SAG} is related to wave energy [*Munk and Sargent*, 1954; *Emery et al*., 1949; *Weydert*, 1979; *Sneh and Friedman*, 1980; *Blanchon and Jones*, 1995]. SAG formations are proposed to induce a cellular circulation serving to transport debris away from the reef along the groove [*Munk and Sargent*, 1954]; however, no field or modeling studies have been carried out to assess this circulation. Although the relationship between SAG orientation and incoming wave orientation, and the relationship between h_{spr}, λ_{SAG}, and incoming wave energy are qualitatively known, the mechanism for these relationships has not been investigated.

[7] The primary purpose of the present work is to examine the hydrodynamics of a typical fore reef system (seaward of the surf zone) with SAG formations to determine the effects of the SAG formations on the shoaling waves and circulation. To address this question, a phase-resolving nonlinear Boussinesq model (section 2) was used with idealized SAG bathymetry and site conditions from Moloka'i, Hawai'i (section 3). The model shows that SAG formations induce Lagrangian circulation cells (section 4.1). A mechanism for this circulation in terms of the momentum balance (section 4.2), the role of various hydrodynamic and geometric parameters (section 4.3), and the effect of spatially variable drag coefficient (section 4.4) are investigated. A discussion follows on the relative effect of an open back reef on the SAG-induced circulation (section 5.1), the hydrodynamics of different SAG wavelengths (section 5.2), and the SAG-induced circulation and potential three-dimensional effects (section 5.3), with conclusions in section 6.

2. Boussinesq Wave and Current Model

[8] A time-dependent Boussinesq wave model, *funwaveC*, which resolves individual waves and parameterizes wave breaking, is used to numerically simulate velocities and sea surface height on the reef [*Feddersen*, 2007; *Spydell and Feddersen*, 2009; *Feddersen et al*., 2011]. The model Boussinesq equations [*Nwogu*, 1993] are similar to the nonlinear shallow water equations but include higher order dispersive terms. The equation for mass (or volume) conservation is

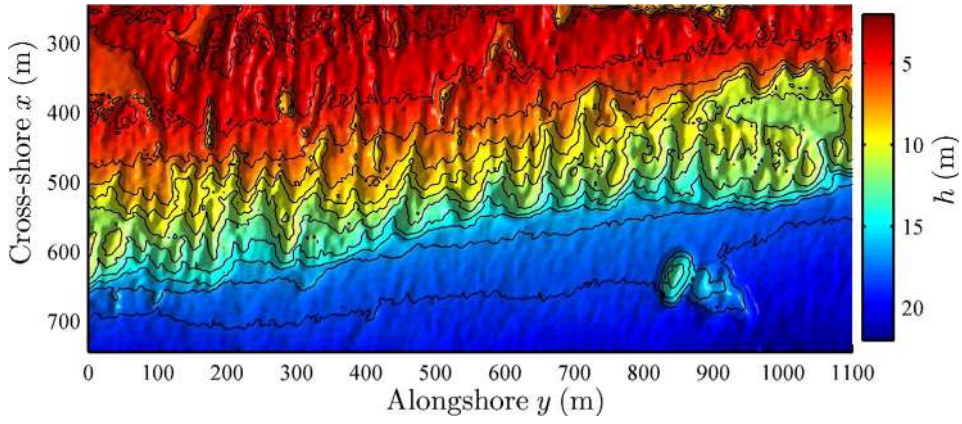

Figure 2. Morphology of characteristic SAG formations off southern Moloka'i, Hawai'i. Contour lines are 2 m spacing. Location is approximately 21°05′N, 157°10′W.

$$\frac{\partial \eta}{\partial t} + \nabla \cdot [(h+\eta)\boldsymbol{u}] + \nabla \cdot \boldsymbol{M}_d = 0, \tag{1}$$

where η is the instantaneous free surface elevation, t is time, h is the still water depth, $\boldsymbol{M}_d$ is the dispersive term, and $\boldsymbol{u}(u, v)$ is the instantaneous horizontal velocity at the reference depth $z_r = -0.531h$ (approximately equal to the depth-averaged velocity for small kh), where $z = 0$ at the still water surface. The momentum equation is

$$\frac{\partial \boldsymbol{u}}{\partial t} + \boldsymbol{u} \cdot \nabla \boldsymbol{u} = -g\nabla\eta + \boldsymbol{F}_d + \boldsymbol{F}_{\mathrm{br}} - \frac{\boldsymbol{\tau_b}}{\rho(h+\eta)} - \upsilon_{\mathrm{bi}} \nabla^4 \boldsymbol{u} - \boldsymbol{F}_s, \tag{2}$$

where g is the gravitational constant, $\boldsymbol{F}_d$ are the higher-order dispersive terms, $\boldsymbol{F}_{\mathrm{br}}$ are the breaking terms, $\boldsymbol{\tau_b}$ is the instantaneous bottom stress, and υ_{bi} is the hyperviscosity for the biharmonic friction ($\nabla^4 \boldsymbol{u}$) term, and $\boldsymbol{F}_s$ is the surface forcing. The dispersive terms $\boldsymbol{M}_d$ and $\boldsymbol{F}_d$ are given by equations (25) and (25) in *Nwogu* [1993]. The bottom stress is parameterized with a quadratic drag law

$$\boldsymbol{\tau_b} = \rho C_d \boldsymbol{u}|\boldsymbol{u}|, \tag{3}$$

with the nondimensional drag coefficient C_d and density ρ. The effect of wave breaking on the momentum equations is parameterized as a Newtonian damping

$$\boldsymbol{F}_{\mathrm{br}} = \frac{1}{(h+\eta)} \nabla \cdot [\upsilon_{\mathrm{br}} (h+\eta) \nabla \boldsymbol{u}], \tag{4}$$

where ν_{br} is the eddy viscosity associated with the breaking waves [*Kennedy et al*., 2000]. When $\partial\eta/\partial t$ is sufficiently large (i.e., the front face of a steep breaking wave), ν_{br} becomes nonzero. Additional details of the *funwaveC* model are described by *Feddersen* [2007], *Spydell and Feddersen* [2009], and *Feddersen et al*. [2011].

[9] Postprocessing of the instantaneous model velocity and sea-surface elevation output were conducted to separate the Eulerian, Lagrangian, and Stokes drift velocities [e.g., *Longuet-Higgins*, 1969; *Andrews and McIntyre*, 1978]:

$$\boldsymbol{U_E} = \overline{\boldsymbol{u}}, \tag{5}$$

$$\boldsymbol{U_L} = \frac{\overline{(h+\eta)\boldsymbol{u}}}{\overline{h+\eta}}, \tag{6}$$

$$\boldsymbol{U_S} = \boldsymbol{U_L} - \boldsymbol{U_E}, \tag{7}$$

where an over bar ($\bar{}$) indicates phase (time) averaging, $\boldsymbol{U_E}(U_E, V_E)$ is the mean Eulerian velocity, $\boldsymbol{U_L}(U_L, V_L)$ is the mean Lagrangian velocity, and $\boldsymbol{U_S}(U_S, V_S)$ is the Stokes drift. This form for $\boldsymbol{U_S}$ is compared to the linear wave theory form in Appendix A. The wave height H can be approximated from the variance of the surface [e.g., *Svendsen*, 2007]:

$$H = \sqrt{8\left(\overline{\eta'^2}\right)}, \tag{8}$$

where $\eta = \overline{\eta} + \eta'$. The mean wave direction θ is given by

$$\tan 2\theta = \frac{2C_{\mathrm{uv}}}{C_{\mathrm{uu}} - C_{vv}}, \tag{9}$$

where the variance (C_{uu}, C_{vv}) and covariance (C_{uv}) are used with a monochromatic wave field and are equivalent to the spectral definition given by *Herbers et al*. [1999], and $\theta = 0$ corresponds to normally incident waves. Although realistic ocean waves are random, monochromatic waves are used here for simplicity and to highlight the linkage of the wave shoaling on SAG bathymetry with the resulting circulation. A cross-shore Lagrangian circulation velocity U_c is defined as

$$U_C = U_L \cos(\varphi), \tag{10}$$

where φ is the angle between the x and y components of $\boldsymbol{U}_L$. In the presence of a strong alongshore current, cross-shore circulation is negligible ($\varphi \approx \pi/2$) and U_c will approach zero; while in the presence of strong cross-shore current ($\varphi \approx 0$), U_c will approach U_L.

[10] Under steady-state mean current conditions, the phase-averaged unsteady ($\partial\boldsymbol{u}/\partial t$) and dispersive ($\boldsymbol{F}_d$) terms in the Boussinesq momentum equations (equation (2)) are effectively zero. Additionally, the velocity $\boldsymbol{u}$ can be decomposed into mean ($\overline{\boldsymbol{u}}$) and wave ($\boldsymbol{u}'$) components, essentially a Reynolds decomposition

$$\boldsymbol{u} = \overline{\boldsymbol{u}} + \boldsymbol{u}', \tag{11}$$

and the phase-averaged nonlinear term of equation (2) becomes (with the use of equation (5))

$$\overline{\boldsymbol{u} \cdot \nabla \boldsymbol{u}} = \overline{(\overline{\boldsymbol{u}} + \boldsymbol{u}') \cdot \nabla (\overline{\boldsymbol{u}} + \boldsymbol{u}')} = \boldsymbol{U_E} \cdot \nabla \boldsymbol{U_E} + \overline{\boldsymbol{u}' \cdot \nabla \boldsymbol{u}'}. \tag{12}$$

[11] The phase-averaged momentum equation can then be written as

$$\boldsymbol{U_E} \cdot \nabla \boldsymbol{U_E} + \overline{\boldsymbol{u}' \cdot \nabla \boldsymbol{u}'} = -g\nabla\overline{\eta} + \overline{\boldsymbol{F}_{\mathrm{br}}} - \overline{\frac{\boldsymbol{\tau_b}}{\rho(h+\eta)}} - \upsilon_{\mathrm{bi}} \nabla^4 \boldsymbol{U_E} - \overline{\boldsymbol{F_S}}. \tag{13}$$

[12] The effect of the waves on the mean Eulerian velocity is given by the nonlinear wave term ($\overline{\boldsymbol{u}' \cdot \nabla \boldsymbol{u}'}$). This is analogous to a radiation stress gradient on the mean Lagrangian velocity, but without the effect of the free surface. The phase-averaged bottom stress follows from equation (3):

$$\overline{\boldsymbol{\tau_b}} = \rho C_d \overline{\boldsymbol{u}|\boldsymbol{u}|}. \tag{14}$$

[13] In a weak current regime, where U_E/σ_u is small, where σ_u^2 is the total velocity variance, and away from the surf zone where $\eta \ll h$, the bottom stress is proportional to the mean velocity, $\overline{\tau_b} \propto \boldsymbol{U_E}$ [*Feddersen et al*., 2000].

3. Model Setup and Conditions

3.1. Model SAG Bathymetry

[14] An idealized and configurable SAG bathymetry for use in numerical experiments was developed based on well-studied SAG formations on the southwestern coast of

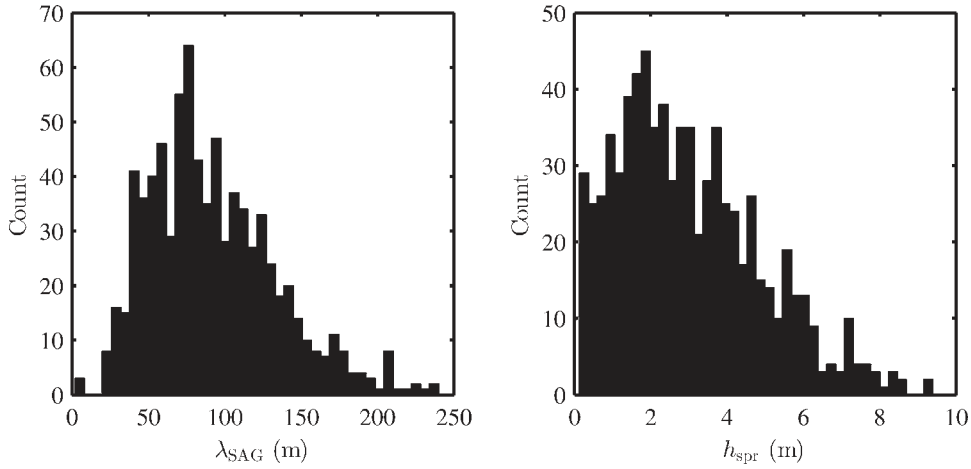

Figure 3. Distribution of SAG wavelength λ_{SAG} and spur height h_{spr} of SAG formations at 5, 10, 15, and 20 m depth alongshore bathymetric profiles from southern Moloka'i, Hawai'i.

Moloka'i, Hawai'i (approximately 21°N, 157°W). High-resolution Scanning Hydrographic Operational Airborne Lidar Survey (SHOALS) laser-determined bathymetry data were used in combination with previous studies in the area [*Field et al*., 2007]. The reef flat, with an approximate 0.3% slope and water depths ranging from 0.3 to 2.0 m, extends seaward from the shoreline to the reef crest (Figure 2, $x < 400$ m) [*Storlazzi et al*., 2011]. Shore-normal ridge-and-runnel structure characterizes the outer reef flat. Offshore of the reef crest, from depths of 3 to 30 m lies the fore reef that is generally characterized by an approximately 7% average slope (β_f) and shore-normal SAG structures covered by highly variable percentages of live coral (Figure 2) [*Storlazzi et al*., 2011]. Note the SAG formations have a roughly coherent λ_{SAG} and cross-shore position, yet with natural variability.

[15] Analysis of the SHOALS bathymetric data used in *Storlazzi et al*. [2003] was conducted, of the fringing reef of southern Moloka'i from Kaunakakai west approximately 18.5 km to the western extent of the island. Alongshore bathymetric profiles taken at the 5, 10, 15, and 20 m depth isobaths were analyzed using a zero crossing method (similar to wave height routines). Of a total 784 measured SAG formations across all depths, the results show a mean λ_{SAG} of 91 m, and a mean h_{spr} of 3.0 m (Figure 3). SAG formations generally had larger λ_{SAG} and h_{spr} at deeper depths, a conclusion also noted in *Storlazzi et al*. [2003].

[16] A selection of 10 prominent SAG formations from this same area of southern Moloka'i, from areas with documented active coral growth in *Field et al*. [2007] was used to further characterize λ_{SAG}, h, W_{grv}, and h_{spr} using alongshore and cross-shore profiles. The geometric shape of the SAG formations was variable, but in general an absolute value of a cosine function well represented the planform alongshore geometry and a skewed Gaussian function well represented the shore-normal profile shape. Adopting a coordinate system of x being positive offshore from the coast, and y being alongshore, the functional form of the idealized depth $h(x, y)$ is given by

$$h(x,y) = h_{base} - h_{spr}\, h_x h_y + \eta_{tide}\,, \tag{15}$$

where $h_{base}(x)$ is the cross-shore reef form with reef flat and fore reef, η_{tide} is the tidal level, and the cross-shore SAG variability $h_x(x)$ and alongshore SAG variability $h_y(y)$ are given by

$$h_x = \exp\left[\frac{-(x-\ \mu\ )^2}{2\varepsilon^2}\right], \tag{16}$$

$$h_y = \max\left[(1+\alpha)|\cos\left(\frac{\pi y}{\lambda_{SAG}}\right)| - \alpha, 0\right], \tag{17}$$

where μ is the x location of peak SAG height, ε is a spreading parameter with $\varepsilon = \varepsilon_1$ for $x \geq \mu$ and $\varepsilon = \varepsilon_2$ for $x < \mu$ to create the skewed Gaussian form, and α is a coefficient depending on W_{grv} and λ_{SAG} given by

$$\alpha = \frac{\left|\cos\left[\frac{\pi}{2}\left(1+\frac{W_{grv}}{\lambda_{SAG}}\right)\right]\right|}{1-\left|\cos\left[\frac{\pi}{2}\left(1+\frac{W_{grv}}{\lambda_{SAG}}\right)\right]\right|}. \tag{18}$$

[17] These equations were used with the typical SAG parameters of $\lambda_{SAG} = 50$ m, $h_{spr} = 2.9$ m, $\mu = 550$ m, $\varepsilon_1 = 77$ m, $\varepsilon_2 = 20$ m, $W_{grv} = 3$ m, and $\eta_{tide} = 0$ (Figure 4). Maximum depth was limited to 22 m based on kh model constraints. Qualitatively, this form is similar to SAG formations in Figure 2, thus giving some confidence that this idealized model bathymetry is representative of SAG formations.

3.2. Model Parameters and Processing

[18] Bottom roughness for the reef was evaluated using the methods of *Lowe et al*. [2009], assuming an average coral size of 14 cm, and thus a drag coefficient $C_d = 0.06$. Similar values of drag coefficients for coral reefs are reported in *Rosman and Hench* [2011]. The base-configuration model had a spatially uniform $C_d = 0.06$, with no C_d variation between spurs and grooves. As grooves often do not have coral but are instead filled with sediment [see Figure 1, and *Storlazzi et al*., 2003], some additional runs were conducted with a spatially variable C_d that was lower ($C_d = 0.01$) in the grooves to determine the

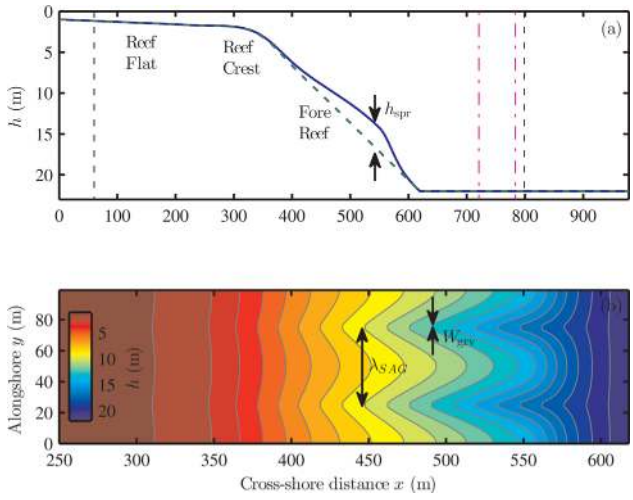

Figure 4. Idealized SAG model domain. (a) *x*-*z* profile, with spur (blue solid), groove (green dash), wave maker (magenta dash-dot), and sponge layers (black dash), (b) *x*-*y* contours. Note difference in cross-shore scale.

potential effect of variable bottom roughness (section 4.4). The $C_d = 0.01$ used for the sand channels was assumed to have higher roughness than for flat sand due to likely sand waves and coral debris.

[19] Typical wind and wave conditions on Moloka'i have been summarized in *Storlazzi et al*. [2011]. In general, wind speed varies from 0 to 20 m/s, and direction is variable depending on the season. Average incident wave conditions are also variable and dependent on the season, but in general from offshore buoy data the average deep-water wave height varies from 0.5 to 1.5 m, average deep-water wave period varies from 6 to 14 s, and average observed deep-water wave angle varies from 0° to 80° (0° corresponds to normally incident waves). The wave angle was assumed to follow Snell's law in propagating from deep-water offshore to the model wave maker at 22 m depth, thus limiting the range of possible θ_i. Tidal variation for southern Moloka'i is 0.4–1.0 m.

[20] A grid size of $\Delta x = \Delta y = 1$ m was used with bathymetry, as shown in Figure 4. Sponge layers were located at 60 and 800 m offshore (Figure 4a). The wave maker center was located at 752 m (Figure 4a), with forcing incident wave height H_i, period T_i and angle θ_i. The computational time step was 0.01 s, and instantaneous values of u, v, η, and ν_{br} were output at 0.2 s intervals. The maximum value of kh in the model domain was 1.1 for the base configuration (offshore) and 1.5 for all runs and is within the limits suggested by *Nwogu* [1993]. A biharmonic eddy viscosity ν_{bi} of 0.2 $\mathrm{m^4\ s^{-1}}$ was used, with wave breaking parameters of $\delta_b = 1.2$, $\eta_t^{(I)} = 0.65\sqrt{gh}$, $\eta_t^{(F)} = 0.15\sqrt{gh}$, and $T^* = 5\sqrt{h/g}$ as defined by *Kennedy et al*. [2000]. Surface forcing due to wind was input to the model assuming a typical drag law in the momentum equation

$$\boldsymbol{F_S} = \boldsymbol{\tau_w}/(h\ \rho\ ) = \frac{C_{\mathrm{dw}}\,\boldsymbol{U_{10}}|\boldsymbol{U_{10}}|\rho_a}{h\ \rho}, \tag{19}$$

where drag $C_{\mathrm{dw}} = 0.0015$, density of air $\rho_a = 1$ kg $\mathrm{m^{-3}}$, and the wind velocity $\boldsymbol{U_{10}}(U_{10}, V_{10})$ at a reference level of 10 m.

[21] The model was first run in a *base configuration* with model parameters typical of average conditions on Moloka'i (Table 1) to diagnose the SAG-induced circulation. Subsequently, the model parameters were varied (denoted *variation models*: Table 1). The variation models configuration is similar to that described previously. However, for θ_i variation, the alongshore length was extended to 700 m to allow the oblique waves to fit into the alongshore domain with periodic boundary conditions. Additionally, for β_f variation the cross-shore dimension was adjusted so that the wave maker and sponge layers were the same distance from the SAG formations. For example, for $\beta_f = 2\%$, the cross-shore domain length was 1692 m, the wave maker was located at $x = 1466$ m, and the sponge at $x = 1512$ m. For variation in T_i, the cross-shore width of the wave maker was held constant at approximately 60 m. For variation in λ_{SAG}, the alongshore model length was adjusted to model $2\lambda_{\mathrm{SAG}}$.

[22] Model run time was 3600 s, with 3240 s of model spin-up and the last 360 s for postprocessing analysis. At the model spin-up time, the mean Eulerian currents at all locations in the model domain had equilibrated. Simulations conducted with variable alongshore domains that are multiples of λ_{SAG} gave identical results, thus an alongshore domain that spanned $2\lambda_{\mathrm{SAG}}$ was used here.

4. Results

4.1. Base-Configuration Model Results

[23] This section describes the idealized base-configuration model based on typical parameters for southern Moloka'i, Hawai'i (Table 1). Results are shown for the model domain from the edge of the onshore sponge layer ($x = 60$ m) to the onshore side of the wave maker ($x = 720$ m). The cross-shore variation of η at the end of the model run ($t = 3600$ s), H, θ, and $\overline{\eta}$, for both the SAG profiles are shown in Figure 5. As the waves approach the fore reef they steepen and increase in height from 1.0 to 1.8 m (trough-to-crest) (Figure 5a) and from 1.0 to 1.3 m (based on surface variance H) (Figure 5b). Within the surf zone (demarked by the vertical dotted lines), the waves were actively breaking, reducing H (Figure 5b). H continues to decay with onshore propagation along the reef flat. H is

Table 1. Parameters Used for Base-Configuration Model and Range of Parameters for Variation Models

Model Variable	Base-Configuration Model	Variation Models Min	Variation Models Max
θ_i (°)	0	0	32.5
H_i (m)	1	0.25	2.5
T_i (s)	10	8	22
η_{tide} (m)	0	−0.9	0.9
U_{10} (m/s)	0	−30	30
V_{10} (m/s)	0	0	30
h_{spr} (m)	2.9	0	8
μ (m)	550	500	600
λ_{SAG} (m)	50	20	240
C_d coral	0.06	0.01	0.12
$W_{\mathrm{grv}}/\lambda_{\mathrm{SAG}}$	0.06	0	0.82
β_f	0.07	0.02	0.13

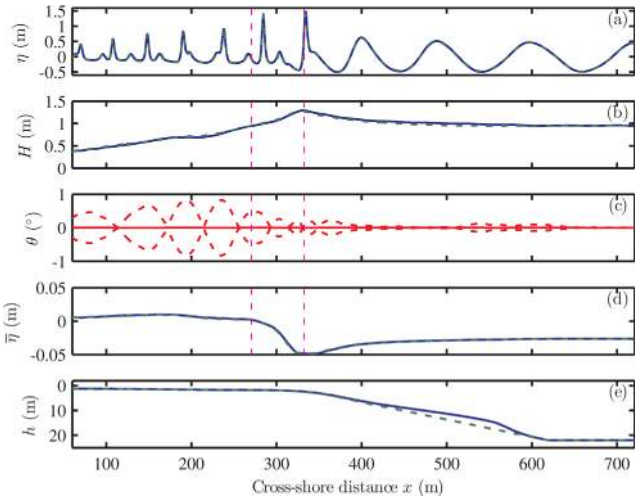

Figure 5. Model surface results for base configuration. (a) Instantaneous surface η ($t = 3600$ s), (b) wave height H, (c) mean alongshore wave angle θ (red solid) and max/min alongshore θ (red dash), (d) mean setup $\overline{\eta}$, and (e) cross-shore depth h. Alongshore location for (a), (b), (d), and (e) at spur $y = 50$ m (blue solid), groove $y = 75$ m (green dash). Vertical lines (magenta dash), indicate surf zone extent.

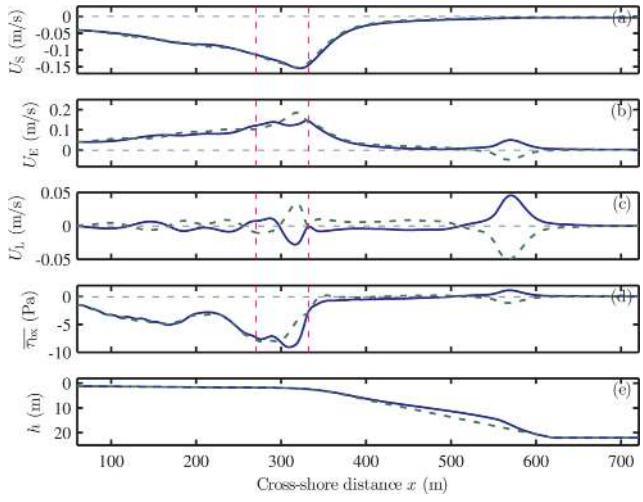

Figure 6. Model velocity and bed shear results for base configuration. (a) Cross-shore Stokes drift U_S, (b) Eulerian velocity U_E, (c) Lagrangian velocity U_L, (d) average cross-shore bed shear stress $\overline{\tau_{bx}}$, and (e) cross-shore depth profile at spur $y = 50$ m (blue solid) and groove $y = 75$ m (green dash). Vertical lines (magenta dash) indicate surf zone extent.

slightly higher along the spur, due to the effects of diffraction and refraction. The alongshore mean θ is nearly zero along the model domain, but the alongshore maximum and minimum θ show small oscillations induced along the reef flat due to effects of diffraction and refraction (Figure 5c). The value $\overline{\eta}$ is slightly set down just before wave breaking, is set up through the surf zone, and is fairly constant on the reef flat (Figure 5d). This cross-shore reef setup profile is qualitatively in agreement with field observations [e.g., *Taebi et al*., 2011; *Monismith*, 2007]. There are very small O (1%) differences in $\overline{\eta}$ between the SAG profiles which are much smaller than the cross-shore variability in $\overline{\eta}$ (i.e., $|\delta\overline{\eta}/\delta y| \ll |\delta\overline{\eta}/\delta x|$).

[24] The cross-shore variation of U_S, U_E, and U_L for both SAG profiles is shown in Figure 6. Positive velocities are oriented offshore and negative velocities are oriented onshore. U_S (computed from equation (7)) increases from offshore to wave breaking and decreases within the surf zone and on the reef flat. Along the SAG system, there is a small O (20%) difference in U_S between the SAG profiles. Model derived U_S (equation (7)) and U_S based on second-order wave theory (i.e., a nonlinear quantity accurate to second order in ak, whose origins are based in linear wave theory, equation (A1)) are similar in the shoaling fore reef region (Appendix A). Along the majority of the fore reef ($350\text{ m} < x < 520$ m), U_E is O (50%) larger over the groove than over a spur (Figure 6b). The circulation U_c is nearly identical to U_L in Figure 6c, due to weak alongshore currents along the SAG profiles in this model. The predominant two-dimensional U_L circulation pattern is onshore flow over the spur and offshore flow over the groove along the majority of the SAG formation up to the surf zone ($330\text{ m} < x < 520$ m) (Figure 7). Near the offshore end of the spur ($x \approx 550$ m), this U_L circulation pattern is reversed, see section 5.3 for further discussion on potential three-dimensional effects.

[25] From offshore, the magnitude of $\overline{\tau_{bx}}$ generally increases up to wave breaking and slowly decreases on the reef flat (Figure 6d). Along the majority of the SAG formation up to the surf zone ($330\text{ m} < x < 520$ m), $\overline{\tau_{bx}}$ is

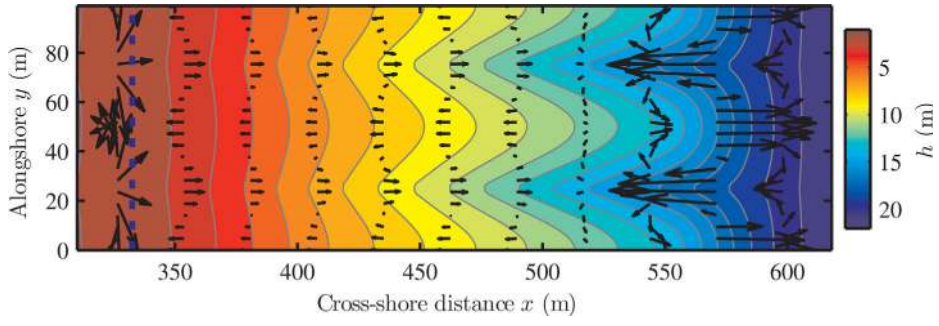

Figure 7. Lagrangian velocity U_L vectors from base configuration and 1 m bathymetric contours zoomed to SAG formations. Maximum velocity vector scale is 0.05m/s, and vertical dashed blue line represents the offshore edge of the surf zone.

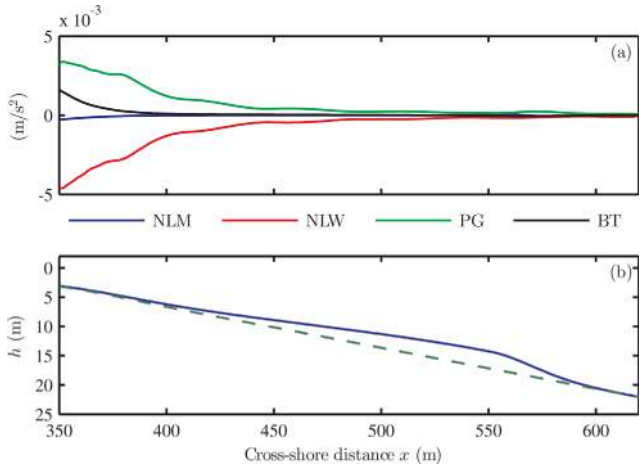

Figure 8. Phase-averaged cross-shore momentum balance for base configuration at top of spur $y = 50$ m. (a) Cross-shore phase-averaged x-momentum significant terms, NLM, NLW, PG, and BT terms, residual error is small, (b) cross-shore depth profile for spur (blue solid) and groove (green dash).

stronger on the spur than the groove and is oriented onshore on the spur, while oscillating sign on the groove.

4.2. Mechanism for Circulation

[26] Outside the surf zone, assuming normally incident waves, steady-state mean velocities, small alongshore currents, and no surface forcing, the phase-averaged cross-shore (x) momentum equation (equation (13)) is given by

$$U_E \frac{\partial U_E}{\partial x} + \overline{u'\frac{\partial u'}{\partial x}} = -g\frac{\partial \overline{\eta}}{\partial x} - \frac{\overline{\tau_{bx}}}{\rho(h+\eta)}, \tag{20}$$

where the terms are referenced from left to right as nonlinear advective mean (NLM), nonlinear advective wave (NLW), pressure gradient (PG), and bottom stress (BT). The remaining terms in equation (13) are negligible (confirmed through model results). The NLW term is analogous to the radiation stress gradient in wave-averaged models [*Longuet-Higgins and Stewart*, 1964] (see Appendix A for comparison of the direct radiation stress estimates with those of second-order wave theory).

[27] The fore reef (400 m $< x <$ 600 m) has a classic set-down balance [e.g., *Bowen*, 1969; *Kumar et al.*, 2011] between PG and NLW terms (Figure 8a). Closer to where wave-breaking occurs (330 m $< x <$ 400 m), BT also becomes important (Figure 8a). Within the surf zone (270 m $< x <$ 330 m) and on the reef flat ($x <$ 270 m), the classic surf zone setup (PG-NLW-F_{br}) and reef-flat (PG-BT) cross-shore momentum balances were obtained from the model [e.g., *Monismith*, 2007].

[28] On the SAG formations (400 m $< x <$ 600 m), the alongshore variation of the cross-shore momentum balance (equation (20)) shows that the PG and NLW terms do not balance and their difference is largely balanced by BT (Figure 9a). The NLM term is very small. The PG and NLW mismatch depends on alongshore position on the SAG bathymetry (Figure 9c). The alongshore variation in NLW is primarily due to the local cross-shore slope, whereas the alongshore variation in PG is primarily due to the local depth (see Appendix B). On the spurs, the PG and NLW terms are basically in balance as in a classic set-down balance [*Bowen*, 1969], whereas on the grooves, they are out of balance, and the PG and NLW mismatch is balanced by the BT. The residual forcing accelerates the flow until BT is large enough to balance it which drives an offshore U_E. U_S is very weakly alongshore variable so the alongshore variation in U_L, and hence the circulation is largely due to U_E (Figure 9b). Note that the fore reef circulation does not depend on wave breaking within the surf zone (confirmed through separate model runs with smaller H_i that did not have a surf zone).

4.3. Effects of Hydrodynamic Conditions and SAG Geometry

[29] The base-configuration parameters were varied in the model (denoted variation models, Table 1) to assess their effect on U_c and $\overline{\tau_{bx}}$ at a reference location ($x_r = 440$ m, $y_r =$ spur top) as a representative location to assess the hydrodynamics. This location captures the main cross-shore U_L circulation cell for a wide range of modeled parameters (e.g., H_i, C_d, and h_{spr}). To evaluate relative changes to U_c and $\overline{\tau_{bx}}$, these are normalized by the base-configuration values at the reference location:

$$\widehat{U_c} = U_c / U_{cb}, \tag{21}$$

$$\widehat{\tau_{bx}} = \overline{\tau_{bx}} / \overline{\tau_{bxb}}, \tag{22}$$

with $U_{cb}(x_r, y_r) = -0.0060$ m/s and $\overline{\tau_{bxb}}\ (x_r, y_r) = -0.37$ Pa, representing the base configuration. The reference water depth h_r is the depth at the reference location $h(x_r, y_r)$. For the variation in slope β_f and cross-shore location μ models, the cross-shore reference location x_r was positioned in the same relative cross-shore position on the SAG formation for each geometric configuration (i.e., base configuration $\mu = 500$ m and $x_r = 440$ m; for $\mu = 550$ m, $x_r = 490$ m).

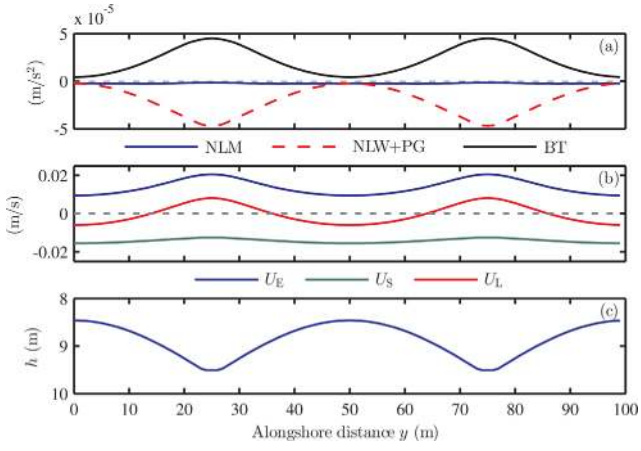

Figure 9. Alongshore variation of x-momentum terms and velocity for base configuration at $x = 440$ m. (a) Alongshore phase-averaged x-momentum significant terms, NLM, NLW + PG, and BT terms, residual error is small, (b) U_E, U_S, and U_L velocities, and (c) depth h.

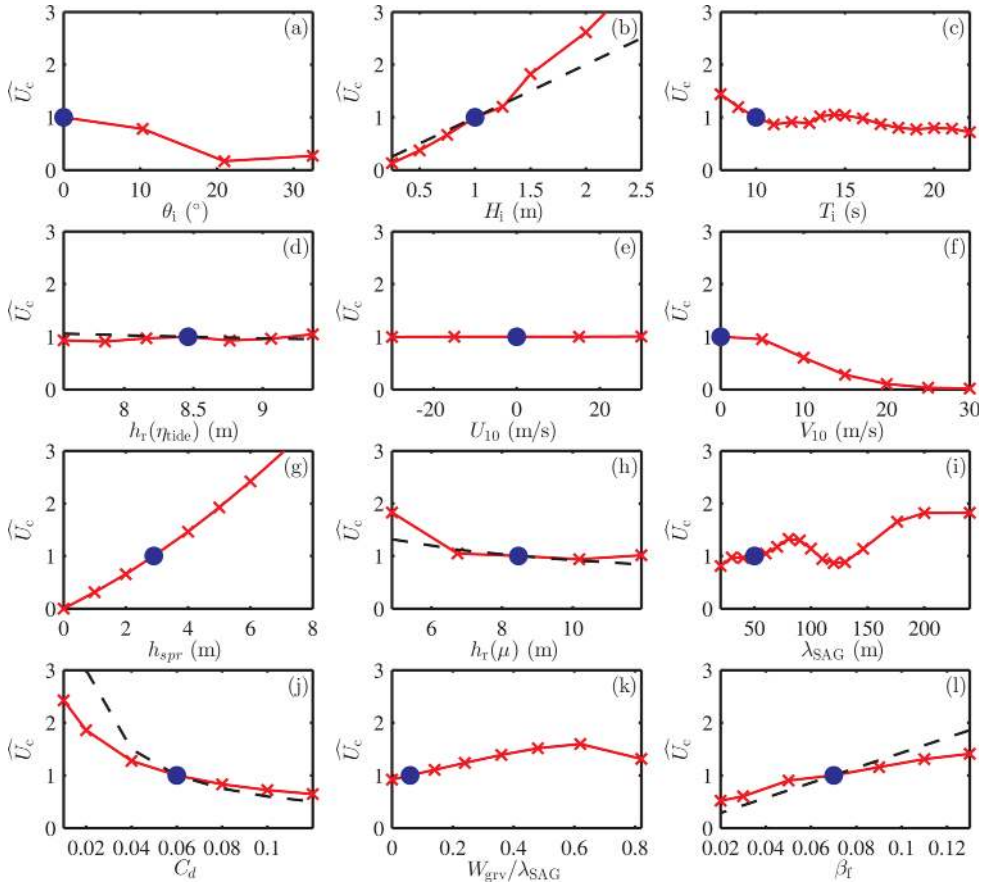

Figure 10. Variation of model parameters and their effect on normalized circulation $\widehat{U_c}$ for model results (red solid) and scaling approximation (equation (25)) (black dash) at $x_r = 440$ m, $y_r = 50$ m (spur) as a function of model variables (a) incident wave angle θ_i, (b) incident wave height H_i, (c) incident wave period T_i, (d) depth as a function of tide level η_{tide}, (e) cross-shore wind U_{10}, (f) alongshore wind V_{10},(g) spur height h_{spr}, (h) depth as a function of cross-shore location μ, (i) SAG wavelength λ_{SAG}, (j) drag coefficient C_d, (k) fraction groove width W_{grv}/λ_{SAG}, and (l) fore reef slope β_f. Scaling approximation only shown on (b, d, h, j, and l), blue circle indicates base configuration.

[30] The modeled dependence of $\widehat{U_c}$ and $\widehat{\tau_{bx}}$ on the model variables are shown in Figures 10 and 11, respectively. From a maximum at a spur-normal wave incidence angle ($\theta_i = 0°$), $\widehat{U_c}$ quickly decreases to nearly zero with oblique incidence ($\theta_i = 20°$), with $\widehat{\tau_{bx}}$ remaining nearly constant (Figures 10a and 11a). $\widehat{U_c}$ and $\widehat{\tau_{bx}}$ increase linearly and quadratically, respectively with increasing H_i (Figures 10b and 11b). Increased T_i slightly decreases $\widehat{U_c}$ but shows oscillations in $\widehat{\tau_{bx}}$ (Figures 10c and 11c). The effects of refraction/diffraction are likely important here. $\widehat{U_c}$ and $\widehat{\tau_{bx}}$ weakly decrease with increasing η_{tide} (Figures 10d and 11d). $\widehat{U_c}$ and $\widehat{\tau_{bx}}$ show no variation with U_{10} as expected due to closed cross-shore boundaries (Figures 10e and 11e). Here, wind and waves are not coupled, so increased wind forcing does not influence wave growth. Increased V_{10} decreases $\widehat{U_c}$ (Figure 10f). The circulation cells driven by the SAG bathymetry (Figure 7) are essentially overwhelmed by the increasingly stronger alongshore current, which decreases $\widehat{U_c}$ proportional to $\cos(\varphi)$ (equation (10)). This is similar to oblique wave incidence. Increased V_{10} shows a slight decrease in $\widehat{\tau_{bx}}$ (Figure 11f).

[31] $\widehat{U_c}$ and $\widehat{\tau_{bx}}$ vary inversely with decreasing h_{spr} (Figures 10g and 11g). Similarly, $\widehat{U_c}$ and $\widehat{\tau_{bx}}$ vary inversely with increasing spur cross-shore position μ (Figures 10h and 11h). The dependence of $\widehat{U_c}$ on λ_{SAG} shows small peaks at 80 and 200 m, whereas $\widehat{\tau_{bx}}$ shows a broad, but weak peak centered around 200 m (Figures 10i and 11i). The hydrodynamics of different λ_{SAG} will be discussed in more detail in section 5.2. Increased reef C_d shows decreased $\widehat{U_c}$ and increased $\widehat{\tau_{bx}}$ (Figures 10j and 11j). Increased W_{grv} to λ_{SAG} ratio shows increased $\widehat{U_c}$ and nearly constant $\widehat{\tau_{bx}}$ (Figures 10k and 11k). $\widehat{U_c}$ and $\widehat{\tau_{bx}}$ linearly increase with β_f (Figures 10l and 11l).

[32] The effect of particular model variables (Table 1) on SAG-influenced U_E and $\widehat{\tau_{bx}}$ on the fore reef can be derived from a simplified scaling (Appendix B) of the dominant cross-shore x-momentum balance (section 4.2),

$$U_E \approx \frac{\pi\sqrt{g}\beta_{AS}H_{AS}}{16C_d\sqrt{h_{AS}}}\left[\frac{\gamma_u^{1/2}\gamma_\beta\gamma_H}{\gamma_h^{1/2}} - \frac{\gamma_\eta\gamma_h^{3/2}\gamma_H}{\gamma_u^{1/2}}\right], \tag{23}$$

$$\overline{\tau_{bx}} \approx \frac{\rho g\beta_{AS}H_{AS}^2}{16h_{AS}}\left[\frac{\gamma_u\gamma_\beta\gamma_H^2}{\gamma_h} - \gamma_\eta\gamma_h\gamma_H^2\right], \tag{24}$$

which are equations (B13) and (B12) in Appendix B, respectively. $(\__{AS})$ and $(\_')$ denote an alongshore average and

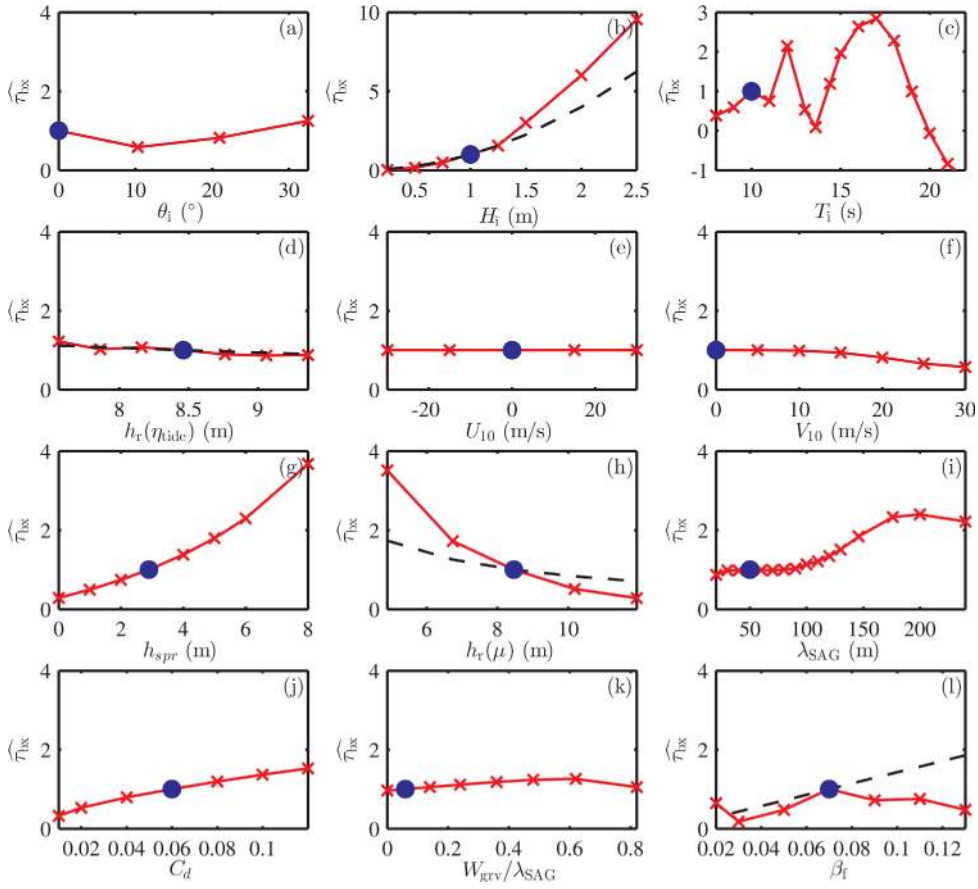

Figure 11. Variation of model parameters and their effect on normalized average cross-shore bottom stress $\widehat{\tau_{bx}}$ for model results (red solid) and scaling approximation (equation (26)) (black dash) at $x_r = 440$ m, $y_r = 50$ m (spur) as a function of model variables (a) incident wave angle θ_i, (b) incident wave height H_i (note larger scale), (c) incident wave period T_i, (d) depth as a function of tide level η_{tide}, (e) cross-shore wind U_{10}, and (f) alongshore wind V_{10}, (g) spur height h_{spr}, (h) depth as a function of cross-shore location μ, (i) SAG wavelength λ_{SAG}, (j) drag coefficient C_d, (k) fraction groove width W_{grv}/λ_{SAG}, and (l) fore reef slope β_f. Scaling approximation only shown on Figures 11b, 11d, 11h, and 11l; blue circle indicates base configuration.

alongshore deviation, respectively. The local depth factor $\gamma_h = 1 + h'/h_{AS}$, γ_β, and γ_H are similarly defined. γ_η and γ_u are kh dependent correction terms defined in Appendix B.

[33] The terms in brackets in equations (23) and (24) contain the local alongshore variability in U_E and $\overline{\tau_{bx}}$; the dominant factors are local depth (γ_h) and local slope (γ_β). Since the strength of U_c is due to alongshore variations in U_E, the nondimensional scaled U_c to first-order scales proportionally to U_E/U_{Eb}, where U_{Eb} is the base condition U_E. Thus, for terms that vary independently in equations (23) and (24), with normally incident waves on the spur, and relatively small h_{spr} $(\beta_{AS} \approx \beta_f)$:

$$\widehat{U_c} \propto \widehat{U_c}\left[\frac{H_i}{H_{ib}}, \frac{\sqrt{h_b}}{\sqrt{h}}, \frac{C_{db}}{C_d}, \frac{\beta_f}{\beta_{fb}}\right], \tag{25}$$

$$\widehat{\tau_{bx}} \propto \widehat{\tau_{bx}}\left[\frac{H_i^2}{H_{ib}^2}, \frac{h_b}{h}, \frac{\beta_f}{\beta_{fb}}\right], \tag{26}$$

where H_{ib}, h_b, C_{db}, and β_{fb} are the base condition H_i, h, C_d, and β_f, respectively. Equations (25) and (26) capture the first-order effects of variables on $\widehat{U_c}$ and $\widehat{\tau_{bx}}$ but do not capture more complex processes such as wave refraction/diffraction, local alongshore-variability of h, H, and β (equations (23) and (24)), as well as other second-order effects ignored in this scaling (such as correlations between η and u' in the BT term). The results for $\widehat{U_c}$ and $\widehat{\tau_{bx}}$ based on the model (equations (21) and (22)) and scaling approximation (equations (25) and (26)) are generally similar (Figures 10b, 10d, 10h, 10j, and 10l and 11b, 11d, 11h, and 11l), with differences likely due to these more complex processes.

4.4. Effect of Spatially Variable Drag Coefficient

[34] The base-configuration model had spatially uniform drag coefficient C_d. However, on typical SAG formations, spurs are covered with hydraulically rough corals (high C_d), while the grooves are often filled with less-rough sediment (low C_d) (example Figure 1). The difference in C_d between spur and groove could also have consequences on the net circulation, independent of SAG geometry. To test this idea, a separate model run was performed with SAG formations ($h_{spr} = 2.9$ m), but with spatially variable C_d

between spurs ($C_d = 0.06$) and grooves ($C_d = 0.01$). A Lagrangian circulation pattern similar to the base configuration (Figure 7) was created, but of slightly larger magnitude (≈4%). In another model run assuming no SAG formations ($h_{spr} = 0$ m) but with spatially variable C_d between spurs ($C_d = 0.06$) and groove ($C_d = 0.01$), a Lagrangian circulation pattern similar to the base configuration (Figure 7) was created, but much smaller, O (10%). Thus, SAG bathymetry is the primary driver of the Lagrangian circulation patterns shown in Figure 7, while alongshore differences in C_d between the coral and sediment-filled grooves have a negligible role. Reef-scale C_d, however, is important to the overall circulation as it sets the magnitude of the circulation (section 4.3).

5. Discussion

5.1. Relative Effect of Return Flow to SAG-Induced Circulation

[35] Many reefs have channels or lagoons onshore of the reef flat with a connection back to the open ocean (open back reef), whereas other reefs have a closed back reef with no ocean connection [*Spalding et al*., 2001]. SAG formations are often found on the fore reefs for both open and closed back-reef geometries. A net onshore flow over reef flats has been measured in numerous field experiments on reefs with such open ocean back connections [*Symonds et al*., 1995; *Bonneton et al*., 2007; *Monismith*, 2007]. The *funwaveC* model has a closed onshore boundary at $x = 0$, which is reasonable for the closed back reef on southern Moloka'i, Hawai'i. A relevant question then is for open back reefs, how strong is the SAG-driven circulation on the fore reef compared to the net onshore flow driven by the open ocean connection?

[36] On the reef flat, neglecting bottom boundary layer wave dissipation, the primary momentum balance on the reef flat is between PG and BT [e.g., *Hearn*, 1999],

$$g(h+\overline{\eta})\nabla\overline{\eta} = -\frac{C_d}{(h+\overline{\eta})^2} q_E |q_E|, \tag{27}$$

where $q_E = (h+\overline{\eta})U_E$ is the mean Eulerian transport. If the overall reef-flat depth change is assumed to be small, the reef-flat flow can be approximated by

$$q_E \cong \left(\frac{gh}{C_d}\right)^{\frac{1}{2}} \left(\frac{\overline{\eta_r} - \overline{\eta_L}}{L_r}\right)^{\frac{1}{2}}, \tag{28}$$

where h is the mean depth on the reef, $\overline{\eta_r}$ is the setup at the end of breaking, $\overline{\eta_L}$ is the mean surface at the lagoon, and L_r is the length of the reef flat. For the modeled base configurations, at the end of model domain where all wave energy is dissipated ($x = 0$ m), the setup $\overline{\eta_r}$ is 0.025 m (not shown in Figure 5), while the offshore ($x = 720$ m) setup $\overline{\eta_L}$ is −0.027 m (Figure 5). Using $C_d = 0.06$, varying L_r from 100 to 2000 m, and varying h from 0.5 to 1.5 m, the results indicate that the q_E has the potential to vary from −0.02 to −0.5 m^2 s^{-1} (directed onshore). The *funwaveC* model results indicate that the SAG formation-induced mean Lagrangian transport [$q_L = (h+\overline{\eta})U_L$] is −0.06 and 0.09 m^2 s^{-1} on the spur and groove, respectively (Figure 6c).

[37] Although this analysis is qualitative, it indicates that it is possible for transport induced over the reef flat to be of a similar magnitude as the SAG-induced circulation. Under certain conditions, such as strong offshore wave forcing inducing strong transport over the reef flat, the onshore transport on the spur would be strengthened, while the offshore transport on the grooves would be reduced or potentially reversed. If there is no reef pass or back channel, that is, a pure fringing reef like at Moloka'i, the SAG-induced circulation will likely be the only fore reef exchange. In all cases, at shallow depths the net Lagrangian flow over the spurs is onshore.

5.2. SAG Wavelength

[38] Waves encountering SAG formations are analogous to the classical problem of waves propagating through a breakwater gap [*Penney and Price*, 1952]. In the latter case, for a breakwater gap less than one wavelength, the waves in the lee of the breakwater propagate approximately as if from a point source; diffraction is predominant within several wavelengths of the gap and further away, refraction dominated [*Penney and Price*, 1952; *Dean and Dalrymple*, 1991]. Although SAG formations are submerged (instead of protruding from the surface), and their alongshore shape is rounded (instead of vertical), wave transformation over SAG formations may have some qualitative similarity to the breakwater gap where $\lambda_{SAG}/2$ corresponds to an approximate gap scale. Thus, for λ_{SAG} much less than the surface gravity wavelength, the wave transformation over the SAG formations may be dominated by diffraction, which tends to alongshore "diffuse" wave height, whereas for λ_{SAG} much larger than the surface gravity wavelength, refraction dominates the wave transformation. For wavelength larger than the gap scale, the effect of refraction becomes important several wavelengths from the end of the spur or approximately 400 m as shown in the oscillations in θ_m for $x < 350$ m (Figure 5c).

[39] For the base configuration, the surface gravity wave wavelength over the SAG formations varied from 115 m (near the front face) to 50 m (near the surf zone). For small $\lambda_{SAG} < 100$ m, the fore reef H difference between the spur and groove is small and grows slowly with λ_{SAG} (Figure 12a) and θ is zero at both spurs and grooves (Figure 12b) consistent with diffraction being dominant. At larger λ_{SAG} (>100 m), the spur-groove difference in H grows rapidly and equilibrates at λ_{SAG} >200 m (Figure 12a). Similarly, the alongshore maximum and minimum θ increases similar to the wave height equilibrating to 5° at $\lambda_{SAG} > 200$ m (Figure 12b). This large λ_{SAG} behavior is consistent with refraction being dominant.

[40] The effect of λ_{SAG} variation on the SAG circulation is seen through the x-momentum terms on the groove which has the largest signal (Figure 13a). The PG and NLW mismatch balanced by BT (section 4.2) increases with λ_{SAG} driving an offshore U_E that also generally increases with λ_{SAG} (Figure 13b). U_S generally increases with λ_{SAG} but has opposite sign of U_E, resulting in U_L (and thus U_c) that has a maximum near $\lambda_{SAG} = 80$ m, with a secondary maximum at larger λ_{SAG} (Figure 13b). $\widehat{\tau_{bx}}$ (Figure 13c) is a function of H^2 (section 4.3). Thus, for λ_{SAG} less than 90 m, $\widehat{\tau_{bx}}$ remains relatively constant, whereas for

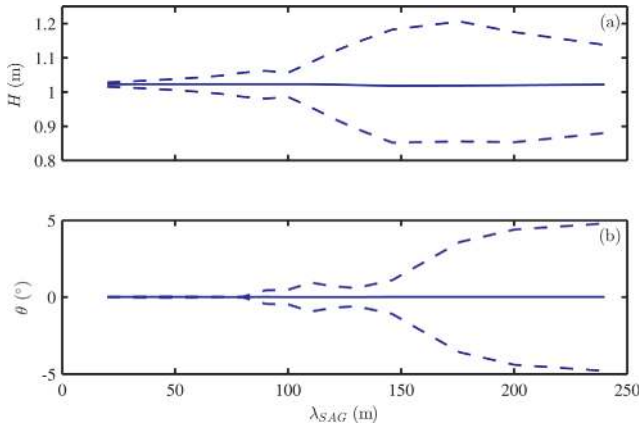

Figure 12. Variation of wave height H and wave angle θ with SAG wavelength λ_{SAG} at $x = 440$ m. (a) Alongshore mean H (solid) and max/min H (dash), (b) alongshore mean θ (solid) and alongshore max/min θ (dash).

larger λ_{SAG}, $\widehat{\tau_{\mathrm{bx}}}$ increases to a local maxima at λ_{SAG} equal to 200 m due to the effects of diffraction/refraction (Figure 13c). It appears the maximum circulation and bottom stress occurs when the SAG wavelength allows for the effects of diffraction to create alongshore differences in wave height without changing the mean wave angle, in which case the SAG formations are most efficient at driving Lagrangian circulation cells.

5.3. Two-Dimensional SAG Circulation and Potential Three-Dimensional Effects

[41] The predominant two-dimensional horizontal Lagrangian circulation pattern induced by the waves is counter-rotating circulation cells. From $x \approx 530$ m to the surf zone, transport is onshore over the spur and offshore over the groove; while from the end of the spur to $x \approx 530$ m the flow direction is reversed (Figure 7). A wide range of hydrodynamic conditions and SAG geometries were modeled (section 4.3). For all modeled conditions except strongly angled waves (high θ) or strong alongshore currents, the waves over SAG formations induce the same basic Lagrangian circulation cells.

[42] The present study focuses on the barotropic (depth-averaged) circulation. The modeled conditions are within the range of values of kh for which the governing equations [*Nwogu*, 1993] and associated numerical methods [*Feddersen*, 2007] are valid. Thus, the depth-averaged flows in this study should be accurate. Even so, it is reasonable to expect three-dimensional flow effects to become important, especially in the deeper areas of the SAG model domain. For example, while the vertical structure of U_S is easily calculated, *funwaveC* only calculates depth-averaged mean Eulerian flows (U_E) meaning that the vertical structure of the mean Lagrangian flows remain to be determined. Additionally, the model does not represent more complicated three-dimensional flow processes such as separation that might occur. Clearly, these more complicated flow features could have important hydrodynamic and biological implications. Thus, further study of the wave-induced currents over the SAG geometry using fully three-dimensional modeling techniques or field studies would seem warranted.

6. Conclusions

[43] In summary, a time-dependent Boussinesq wave model, *funwaveC* that resolves individual waves and parameterizes wave breaking was used to numerically simulate current velocities and sea surface height along SAG formations based on idealized bathymetry from Moloka'i, Hawai'i. The predominant two-dimensional Lagrangian circulation pattern is counterrotating circulation cells induced by the shoaling wave field over the SAG bathymetry. In shallow depths, transport is directed onshore over the spur and offshore over the groove, while near the end of the spur in deeper water the circulation is reversed. The primary driver of these Lagrangian circulation patterns is the waves interacting with the SAG bathymetry, not alongshore differences in bottom drag due to variation in a drag coefficient. The dominant phase-averaged momentum balance is between PG and NLW terms on the fore reef. The alongshore variation of the x-momentum terms shows that the PG and NLW terms are not in exact balance and their difference is balanced by BT.

[44] The effect of model variables on circulation U_c and cross-shore average bottom stress, $\widehat{\tau_{\mathrm{bx}}}$ on the fore reef was approximated using scaling arguments of the dominant cross-shore x-momentum balance. The model results show U_c varies approximately proportionally to H_i, $h^{-1/2}$, C_d^{-1}, and β_f consistent with a simple scaling. The parameters that created the strongest U_c were spur-normal incident waves ($\theta_i = 0°$), increased H_i, no alongshore currents, and increased h_{spr}.

[45] The present study focuses on the barotropic (depth-averaged) circulation, but it is reasonable to expect three-dimensional flow effects to become important, especially in the deeper areas of the SAG model domain. Thus, further

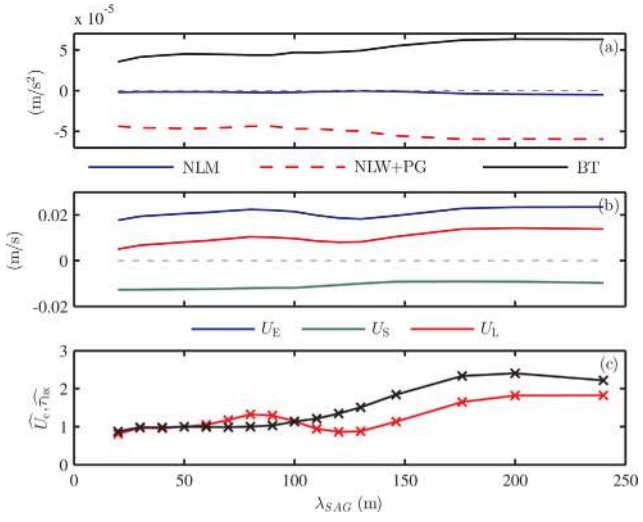

Figure 13. Variation of x-momentum terms, velocity, circulation, and average bottom shear with SAG wavelength λ_{SAG} at $x = 440$ m. (a) Phase-averaged x-momentum significant terms NLM, NLW + PG, and BT; residual error is small, at groove $y = 1.5\lambda_{\mathrm{SAG}}$. (b) U_E, U_S, and U_L velocities, at groove $y = 1.5\lambda_{\mathrm{SAG}}$ and (c) normalized circulation $\widehat{U_c}$ (red) and normalized bottom shear stress $\widehat{\tau_{\mathrm{bx}}}$ (black), at spur $y = \lambda_{\mathrm{SAG}}$.

study of the wave-induced currents over the SAG geometry using fully three-dimensional modeling techniques or field studies is a logical next step.

[46] Many reefs have channels or lagoons onshore of the reef flat with a connection back to the open ocean, whereas other reefs have a closed back reef with no connection [*Spalding et al*., 2001]. Using an order of magnitude analysis, results indicate that it is possible for flow induced over the reef flat to be of a similar magnitude as the circulation induced by the SAG formations. Under all onshore reef flows at shallow depths, the net Lagrangian flow over the spurs remains directed onshore.

[47] An investigation was conducted into the hydrodynamic behavior of SAG formations of different SAG wavelength. It appears the maximum circulation and low bottom stress occurs when the SAG wavelength allows for the effects of diffraction to create alongshore differences in wave height without changing the mean wave angle, thus the SAG formations are most efficient at driving Lagrangian circulation cells.

[48] The typical circulation pattern noted in this study likely brings low-sediment, high "food" water from the open ocean up over the corals on the spur; while simultaneously transporting coral debris and sediment from the surf zone and reef flat along the groove sand channels and away from the reef (assuming low alongshore exchange between spurs and grooves). Average cross-shore bottom shear stress is stronger on the spur than the groove, thus for large wave events that generate shear stress above the capacity of the corals, the corals on the spur would exceed their capacity and break. However, the increased bottom stress on the spur also likely allows for sediment shedding toward the grooves and possibly more nutrient exchange due to increased turbulence on the spur under certain conditions. Thus, while the net effect of bottom shear stress on coral growth remains unclear, increased circulation may favor growth on the coral spur and inhibit coral growth in the groove. Based on variations in the assumed model parameters, some of the strongest factors affecting SAG circulation include spur-normal waves ($\theta = 0°$), increased wave height, and increased spur height. If increased circulation is favorable to coral growth, the modeling results are qualitatively consistent with field observations that SAG formations are orthogonal to typical predominant incident wave angle and are largest and most well developed in areas of larger incident waves [*Munk and Sargent*, 1954; *Roberts*, 1974; *Storlazzi et al*., 2003].

Appendix A: Comparison to Second-Order Wave Theory

[49] It is of practical interest to compare the Stokes drift and radiation stress obtained from second-order wave theory (i.e., nonlinear quantities accurate to second order in *ak*, whose origins are in linear wave theory) to the results obtained from the nonlinear Boussinesq model. The Stokes drift can be approximated from the wave height, assuming second-order wave theory by *Svendsen* [2007]:

$$U_S = \frac{gkH^2}{8h\omega}\cos\theta, \tag{A1}$$

where U_S is in the x direction, H is the wave height, k is the wavenumber, and ω is the wave radian frequency which are related in the usual dispersion relation ($\omega^2 = gk\tanh kh$). The results for U_S using H (equation (A1)) and the difference in Eulerian and Lagrangian velocities (equation (7)) methods have fairly good agreement offshore of wave breaking ($x > 350$ m), where the waves are weakly nonlinear (Figure A1a). Agreement is poor in the surf zone and reef flat due to strong nonlinearity in the wave field (Figure 5a).

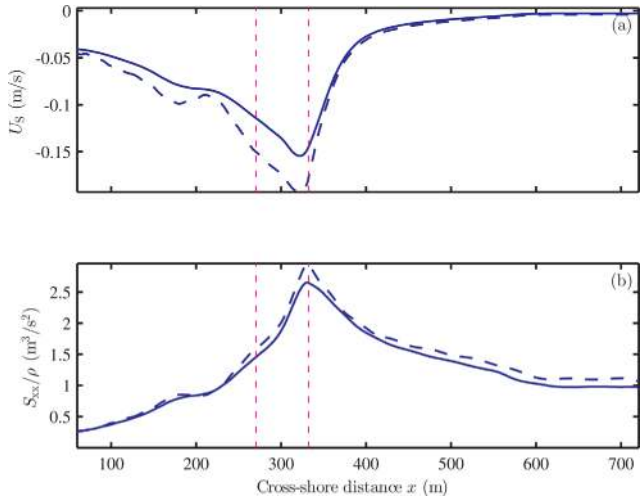

Figure A1. Comparison of cross-shore Stokes drift U_S and radiation stress S_{xx} for base configuration at top of spur $y = 50$ m; (a) U_S obtained directly from the model equation (7) (blue solid), and using linear wave theory equation (A1) (blue dash); and (b) S_{xx} from instantaneous velocities and η equation (A3) (blue solid), and linear wave theory equation (A(4)) (blue dash). Vertical lines (magenta dash) indicate surf zone.

[50] The radiation stress tensor $\boldsymbol{S}_{ij}$ correct to $O(H/L)^3$ is given by *Mei et al*. [2005]:

$$\boldsymbol{S}_{ij} = \rho\int_{-h}^{\eta}\overline{\boldsymbol{u}_i'\boldsymbol{u}_j'}\,\mathrm{d}z + \delta_{ij}\left\{\frac{\rho g}{2}\overline{\eta'^2} - \rho\int_{-h}^{\eta}\overline{w'^2}\,\mathrm{d}z\right\}, \tag{A2}$$

where L is the wavelength ($k/2\pi$) and $\boldsymbol{u}'$ is based on $\boldsymbol{u}' = \boldsymbol{u} - \boldsymbol{U_L}$. For the nonlinear model dynamics, $\boldsymbol{S}_{ij}$ can be approximated by assuming linear wave theory for the third term for vertical velocity w' above, and using the instantaneous depth-averaged velocities, which can account for weak reflections:

$$\boldsymbol{S}_{ij} = \rho\overline{(\eta + h)\boldsymbol{u}_i'\boldsymbol{u}_j'} + \delta_{ij}\frac{\rho g}{2}\overline{\eta'^2}\left(\frac{2kh}{\sinh 2kh}\right), \tag{A3}$$

[51] Equation (A3) can be evaluated from the model results assuming the frequency is known. For progressive waves S_{11} (S_{xx}) is given by *Longuet-Higgins and Stewart* [1964]:

$$S_{11} = S_{xx} = \frac{E}{2}\left[\frac{2C_g}{C}\cos^2\theta + \left(\frac{2C_g}{C} - 1\right)\right], \tag{A4}$$

where E is the energy, C is the phase velocity, C_g is the group velocity, and θ is the wave angle. While the

magnitude of S_{xx} from the two methods is similar (Figure A1b), the results from linear wave theory show more local variability in the cross-shore gradient of S_{xx} (i.e., $\partial S_{xx}/\partial x$) which is the result of small cross-shore oscillations in H (Figure 5b).

Appendix B: Scaling of the Boussinesq Equation

[52] Here, we present an approximate scaling for the SAG circulation developed to help explain the results in section 4.3. The circulation is given by $U_c = (U_E + U_S)\cos(\varphi)$ (equation (10)). The alongshore variation in U_L (and thus U_c) is primarily a result of alongshore variation in U_E, not U_S (which is nearly alongshore uniform) (section 4.2). Thus, to first order, the strength of U_c is due to alongshore variations in U_E.

[53] On the fore reef, away from the surf zone ($\eta \ll h$), but not too deep ($kh < 1.5$), the primary phase-averaged cross-shore (x) momentum balance (equation (20)) is among NLW, PG, and BT (Figure 8a).

$$\overline{u'\frac{\partial u'}{\partial x}} \approx -g\frac{\partial \overline{\eta}}{\partial x} - \overline{\frac{\tau_{bx}}{\rho\,(h+\eta)}}, \tag{B1}$$

[54] Linear wave theory is assumed for normally incident ($\theta = 0$) waves of the form $\eta = (H/2)\cos(\omega t)$, with wave speed C can be expressed as $C = \omega/k = \sqrt{\gamma_c g h}$, where using the dispersion relation $\omega^2 = gk\tanh kh$, a correction to the shallow water wave speed is $\gamma_c = \tanh(kh)/(kh)$. Taking the standard form for linear wave velocity u' [e.g., *Dean and Dalrymple*, 1991] is evaluated at $z_r = -\alpha h$, with $\alpha = 0.531$ [*Nwogu*, 1993]. The wave velocity is then

$$u' = U_0\cos(\omega t), \tag{B2}$$

where $U_0 = \left(\sqrt{g\gamma_u}H\right)/\left(2\sqrt{h}\right)$, and the kh-dependent wave velocity terms are combined

$$\gamma_u = \cosh^2[(1-\alpha)kh]\frac{2kh}{\sinh(2kh)}. \tag{B3}$$

[55] For small kh, $\gamma_u = 1$, for $kh = 1$, $\gamma_u = 0.68$. The NLW wave term from equation (B1) can then be evaluated using equation (B2),

$$\overline{u'\frac{\partial u'}{\partial x}} = \frac{g\gamma_u H}{16h^2}\left[2h\frac{\partial H}{\partial x} - H\frac{\partial h}{\partial x}\right], \tag{B4}$$

where $\partial\gamma_u/\partial x$ is very small [$O(2kh\omega\beta/\sqrt{gh}) \sim O$ (10^{-3} m^{-1}) confirmed through model results and first-order scaling. The mean set-down for alongshore-uniform bathymetry in a classic PG-radiation stress balance offshore of the surf zone is given by $\overline{\eta} = -(kH^2)/[8\sinh(2kh)]$ [*Longuet-Higgins and Stewart*, 1962; *Bowen*, 1969]. This solution is based on alongshore-uniform bathymetry, therefore is it most appropriate that k and h are taken as the alongshore average denoted by k_{AS} and h_{AS}, respectively. The set-down can then be written as

$$\overline{\eta} = -\frac{\gamma_\eta H^2}{16h_{AS}}, \tag{B5}$$

where the kh dependent set-down terms are given by $\gamma_\eta = (2k_{AS}h_{AS})/\sinh(2k_{AS}h_{AS})$. For small kh, $\gamma_\eta = 1$, for $kh = 1$, $\gamma_\eta = 0.55$. The modeled mean set-down was well approximated by equation (B5). The PG term from equation (B1) is then evaluated using equation (B5),

$$g\frac{\partial \overline{\eta}}{\partial x} = -\frac{g\gamma_\eta H}{16h_{AS}^2}\left[2h_{AS}\frac{\partial H}{\partial x} - H\frac{\partial h_{AS}}{\partial x}\right], \tag{B6}$$

where $\partial\gamma_\eta/\partial x$ is very small [$O(2k_{AS}h_{AS}\omega\beta_{AS}/\sqrt{gh_{AS}}) \sim O$ (10^{-3} m^{-1}) confirmed through model results and first-order scaling]. Let the local slope $\partial h/\partial x$ and alongshore average slope $\partial h_{AS}/\partial x$ be denoted by β and β_{AS}, respectively (note for small h_{spr}, $\beta_{AS} \approx \beta_f$). The sum of NLW and PG terms (equations (B4) and (B6)) can be rearranged into two terms, ignoring common terms, one with $\partial H/\partial x\left(h^{-1} - h_{AS}^{-1}\right)$ and the second with $(H/2h)\left(-h^{-1}\beta + h/h_{AS}^2\,\beta_{AS}\right)$. The first is much smaller than the second (confirmed through model results) since $\partial H/\partial x$ is much smaller than $H/2h$ and differences in local versus alongshore depths are linear in the first term, but squared in the second. The sum of NLW and PG terms becomes

$$\overline{u'\frac{\partial u'}{\partial x}} + g\frac{\partial \overline{\eta}}{\partial x} \approx \frac{g\gamma_u\beta H^2}{16h^2}\left[-1 + \left(\frac{\gamma_\eta\beta_{AS}h^2}{\gamma_\eta\beta h_{AS}^2}\right)\right]. \tag{B7}$$

[56] The modeled NLW + PG was reasonably approximated by equation (B7). For purposes of scaling, the BT term in equation (B1) is approximated by

$$\overline{\frac{\tau_{bx}}{\rho(h+\eta)}} \approx \frac{\overline{\tau_{bx}}}{\rho h}, \tag{B8}$$

where it is assumed $h \gg \eta$. Combining equations (B1), (B7), and (B8) with some rearrangement yields

$$\overline{\tau_{bx}} \approx \frac{\rho g\gamma_u\beta H^2}{16h}\left[1 - \left(\frac{\gamma_\eta\beta_{AS}h^2}{\gamma_\eta\beta h_{AS}^2}\right)\right], \tag{B9}$$

where the terms in the large bracket above come from the NLW and PG terms, respectively. In a weak current, small angle regime, where $u' \gg U_E$ is small, for monochromatic, unidirectional waves, the mean bottom stress $\overline{\boldsymbol{\tau_b}}$ is commonly parameterized by [e.g., *Feddersen et al.*, 2000]:

$$\overline{\boldsymbol{\tau_b}} \approx (4/\pi)\rho C_d U_0 \boldsymbol{U_E}, \tag{B10}$$

[57] Combining equations (B9) and (B10) with some rearrangement yields,

$$U_E \approx \frac{\pi\sqrt{g\gamma_u}\beta H}{16C_d\sqrt{h}}\left[1 - \left(\frac{\gamma_\eta\beta_{AS}h^2}{\gamma_u\beta h_{AS}^2}\right)\right], \tag{B11}$$

where the terms in the large bracket above come from the NLW and PG terms respectively.

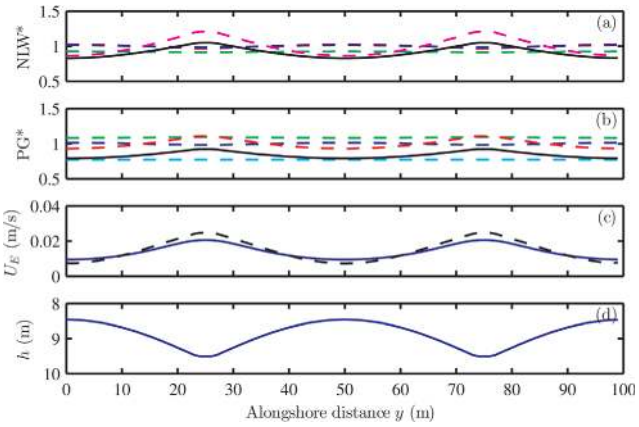

Figure B1. Comparison of alongshore contribution to NLW* and PG* terms and results for U_E from model and scaling at $x = 440$ m; (a) contribution to NLW* term in equation (B13) (black solid) from γ_β (magenta dash), γ_H (blue dash), γ_u (green dash), and γ_h (red dash); (b) contribution to PG* term in equation (B13) (black solid) from γ_η (cyan dash), γ_H (blue dash), γ_u (green dash), and γ_h (red dash); (c) comparison of U_E from model (blue solid) and scaling approximation (equation (B13)) (black dash); and (d) depth h.

[58] Separating alongshore variable h, H, and β into an alongshore average ($\_{\rm AS}$) and a local alongshore deviation ($\_'$) yields, $h = h_{\rm AS} + h' = h_{\rm AS}\gamma_h, H = H_{\rm AS} + H' = H_{\rm AS}\gamma_H,$, and $\beta_{\rm AS} + \beta' = \beta_{\rm AS}\gamma_\beta,$, where the local depth, local wave height, and local slope factors are given by $\gamma_h = 1 + h'/h_{\rm AS}, \gamma_H = 1 + H'/H_{\rm AS}, \gamma_\beta = 1 + \beta'/\beta_{\rm AS}$ respectively. Substituting these expressions into equations (B9) and (B11) and rearranging so that all alongshore variability (i.e., γ_h, γ_H, γ_β, and γ_u) is in the parentheses yields,

$$\overline{\tau_{bx}} \approx \frac{\rho g \beta_{\rm AS} H_{\rm AS}^2}{16 h_{\rm AS}} \left[\frac{\gamma_u \gamma_\beta \gamma_H^2}{\gamma_h} - \gamma_\eta \gamma_h \gamma_H^2 \right], \tag{B12}$$

$$U_E \approx \frac{\pi \sqrt{g} \beta_{\rm AS} H_{\rm AS}}{16 C_d \sqrt{h_{\rm AS}}} \left[\frac{\gamma_u^{1/2} \gamma_\beta \gamma_H}{\gamma_h^{1/2}} - \frac{\gamma_\eta \gamma_h^{3/2} \gamma_H}{\gamma_u^{1/2}} \right]. \tag{B13}$$

[59] The first term in brackets of equation (B13) originates from the NLW term and is denoted NLW* (note change of sign in NLW from Figure 8a), while the second originates from the PG term and is denoted PG*. The alongshore variability in NLW* is most affected by γ_β while γ_u, γ_H, and γ_h have a minor effect (Figure B1a). The alongshore variability in PG* is most affected by γ_h with little to no effect from γ_η, γ_H, and γ_u (Figure B1b). Thus, the alongshore variability in U_E (and thus U_c) is primarily the result of a mismatch between the local slope coefficient γ_β and the local depth coefficient γ_h to the 3/2 power. The alongshore variation in U_E shows good agreement between model results and equation (B13) (Figure B1c).

[60] Equation (B13) is highly approximate to $O\,(H/h)^2$, but explains to first order the U_c dependence on model parameters, as discussed in section 4.3. Note that if the bathymetry is alongshore uniform ($\gamma_\eta = \cosh^2[(1-\alpha)kh]\gamma_u$, $\gamma_h = \gamma_H = \gamma_\beta = 1$) and equation (B13) will predict alongshore uniform $U_E > 0$ (directed offshore); in this case, second-order effects ignored in this scaling would become important.

[61] **Acknowledgments.** The authors are grateful to Oliver Fringer for assistance with modeling, Rob Dunbar for constructive discussions, two anonymous reviewers, as well as Robert Arthur, Jamie Dunckley, Joshua Logan, Lianna Samuel, Sean Vitousek, Ryan Walter, Phillip Wolfram, and Simon Wong. This research was made with government support under and awarded by the U.S. Department of Defense, Office of Naval Research, National Defense Science and Engineering Graduate (NDSEG) Fellowship, 32 CFR 168a. Additional financial support came from the National Science Foundation and the Singapore Stanford Partnership.

References

Acevedo, R., J. Morelock, and R. A. Olivieri (1989), Modification of coral reef zonation by terrigenous sediment stress, *Palaios*, *4*, 92–100, doi:10.2307/3514736.

Andrews, D., and M. McIntyre (1987), An exact theory of waves on Lagrangian mean flow, *J. Fluid Mech.*, *89*, 609–646, doi:10.1017/S0022112078002773.

Atkinson, M. J., and R. W. Bilger (1992), Effect of water velocity on phosphate uptake in coral reef-flat communities, *Limnol. Oceanogr.*, *37*, 273–279, doi:10.4319/lo.1992.37.2.0273.

Blanchon, P., and B. Jones (1995), Marine-plantation terraces on the shelf around Grand Cayman: A result of stepped Holocene sea-level rise, *J. Coastal Res.*, *11*, 1–33.

Blanchon, P., and B. Jones (1997), Hurricane control on shelf-edge-reef architecture around Grand Cayman, *Sedimentology*, *44*, 479–506, doi:10.1046/j.1365–3091.1997.d01–32.x.

Bonneton, P., J.-P. Lefebvre, P. Bretel, S. Ouillon, and P. Douillet (2007), Tidal modulation of wave-setup and wave-induced currents on the Abore coral reef, New Caledonia, *J. Coastal Res. (special issue)*, *50*, 762–766.

Bowen, A. J. (1969), Rip currents: 1. Theoretical investigations, *J. Geophys. Res.*, *74*, 5467–5478, doi:10.1029/JC074i023p05467.

Buddemeier, R. W., and D. Hopley (1998), Turn-ons and turn-offs: Causes and mechanisms of the initiation and termination of coral reef growth, paper presented at the 6th International Coral Reef Symposium, Townsville, Australia.

Carpenter, R. C., J. M. Hackney, and W. H. Adey (1991), Measurements of primary productivity and nitrogenase activity of coral reef algae in a chamber incorporating oscillatory flow, *Limnol. Oceanogr.*, *36*, 40–49, doi:10.4319/lo.1991.36.1.0040.

Chappell, J. (1980), Coral morphology, diversity and reef growth, *Nature*, *286*, 249–252, doi:10.1038/286249a0.

Cloud, P. E. (1959), Geology of Saipan, Mariana Islands, Part 4—Submarine topography and shallow-water ecology, *U. S. Geol. Surv. Prof. Paper 280-K*, pp. 361–445.

Darwin, C. H. (1842), *The Structure and Distribution of Coral Reefs*, p. 207, Smith, Elder and Co., London, U. K.

Dean, R. G., and R. A. Dalrymple (1991), Water wave mechanics for engineers and scientists, in *Advanced Series on Ocean Engineering*, vol. *2*, World Scientific, Hackensack, N. J.

Dennison, W. C., and D. J. Barnes (1988), Effect of water motion on coral photosynthesis and calcification. *J. Exp. Mar. Biol. Ecol.*, *115*, *67–77*, doi:10.1016/0022–0981(88)90190-6.

Emery, K. O., J. I. Tracy, and L. S. Ladd (1949), Submarine geology and topography in the northern Marshall Islands, *Eos Trans. AGU*, *30*, 55–58.

Fabricius, K. E. (2005), Effects of terrestrial runoff on the ecology of corals and coral reefs: Review and synthesis, *Mar. Pollut. Bull.*, *50*(2), 125–146, doi:10.1016/j.marpolbul.2004.11.028.

Feddersen, F. (2007), Breaking wave induced cross-shore tracer dispersion in the surf zone: Model results and scalings, *J. Geophys. Res.*, *112*, C09012, doi:10.1029/2006JC004006.

Feddersen, F., R. T. Guza, S. Elgar, and T. Herbers (2000), Velocity moments in alongshore bottom stress parameterizations, *J. Geophys. Res.*, *105*(C4), 8673–8686, doi:10.1029/2000JC900022.

Feddersen, F., D. B. Clark, and R. T. Guza (2011), Modeling surf zone tracer plumes: 1. Waves, mean currents, and low-frequency eddies, *J. Geophys. Res.*, *116*, C11027, doi:10.1029/2011JC007210.

Field, M., S. Cochran, J. Logan, and C. Storlazzi (2007), The Coral Reef of South Moloka'i, Hawaii, Portrait of a sediment-threatened fringing reef, USGS Sci. Invest. Rep. 2007–5101.

Fortes, M. (2000), The effects of siltation on tropical coastal ecosystems, in *Oceanographic Processes of Coral Reefs*, edited by E. Wolanski, pp. 93–112, CRC Press, Boca Raton, Fla.

Geister, J. (1977), The influence of wave exposure on the ecological zonation of Caribbean coral reefs: Miami, Florida, paper presented at the 3rd International Coral Reef Symposium, Miami, Fla.

Genin, A., S. G. Monismith, M. A. Reidenbach, G. Yahel, and J. R. Koseff (2009), Intense benthic grazing in a coral reef, *Limnol. Oceanogr. 54*(3), 938–951, doi:10.4319/lo.2009.54.3.0938.

Goreau, T. F. (1959), The ecology of Jamaican coral reefs, 1—Species composition and zonation, *Ecology*, *40*, 67–90, doi:10.2307/1929924.

Hearn, C. J. (1999), Wave-breaking hydrodynamics within coral reef systems and the effect of changing relative sea level, *J. Geophys. Res.*, *104*(C12), 30,007–30,019, doi:10.1029/1999JC900262.

Herbers, T., S. Elgar, and R. T. Guza (1999), Directional spreading of waves in the nearshore, *J. Geophys. Res.*, *104*(C4), 7683–7693, doi:10.1029/1998JC900092.

Kan, H., N. Hori, and K. Ichikawa (1997), Formation of a coral reef-front spur, *Coral Reefs*, *16*(1), 3–4, doi:10.1007/s003380050052.

Kennedy, A. B., Q. Chen, J. T. Kirby, and R. A. Dalrymple (2000), Boussinesq modeling of wave transformation, breaking, and runup. I: 1d, *J. Waterw. Port Coastal Ocean Eng.*, *126*(1), 39–47, doi:10.1061/(ASCE)0733–950X(2000)126:1(39).

Kumar, N., G. Voulgaris, and J. Warner (2011), Implementation and modification of a three-dimensional radiation stress formulation for surf zone and rip-current applications, *Coastal Eng.*, *58*, 1097–1117, doi:10.1016/j.coastaleng.2011.06.009.

Longuet-Higgins, M. S. (1969), On the transport of mass by time-varying ocean currents, *Deep Sea Res. Ocean. Abstracts*, *16*, 431–447, doi:10.1016/0011–7471(69)90031-X.

Longuet-Higgins, M., and R. Stewart (1962), Radiation stress and mass transport in gravity waves, with application to 'surf beats', *J. Fluid Mech.*, *13*, 481–504, doi:10.1017/S0022112062000877.

Longuet-Higgins, M., and R. Stewart (1964), Radiation stresses in water waves; a physical discussion, with applications, *Deep-Sea Reas.*, *11*(4), 529–562, doi:10.1016/0011–7471(64)90001-4.

Lowe, R. J., J. L. Falter, S. G. Monismith, and M. J. Atkinson (2009), Wave-driven circulation of a coastal reef-lagoon system, *J. Phys. Oceanogr.*, *39*, 873–893, doi:10.1175/2008JPO3958.1.

Masselink, G., and M. G. Hughes (2003), *Introduction to Coastal Processes and Geomorphology*, p. 354, Oxford Univ. Press, New York.

Mei, C., M. Stiassnie, and D. Yue (2005), *Theory and Applications of Ocean Surface Waves. Advanced Series on Ocean Engineering*, vol. *23*, World Scientific, Hackensack, N. J.

Monismith, S. G. (2007), Hydrodynamics of coral reefs, *Annu. Rev. Fluid Mech.*, *39*, 37–55, doi:10.1146/annurev.fluid.38.050304.092125.

Munk, W. H., and M. C. Sargent (1954), Adjustment of Bikini Atoll to ocean waves, *U. S. Geol. Sur. Prof. Paper 260-C*, pp. 275–280.

Nwogu, O. (1993), Alternative form of Boussinesq equations for nearshore wave propagation, *J. Waterw. Port Coastal Ocean Eng.*, *119*, 618–638, doi:10.1061/(ASCE)0733–950X(1993)119:6(618).

Odum, H. T., and E. P. Odum (1955), Trophic structure and productivity of a windward coral reef community on Eniwetok Atoll, *Ecol. Monogr.*, *25*, 291–320.

Ogston, A., C. Storlazzi, M. Field, and M. Presto (2004), Sediment resuspension and transport patterns on a fringing reef flat, Molokai, Hawaii, *Coral Reefs*, *23*(4), 559–569, doi:10.1007/s00338-004-0415-9.

Penney, W. G., and A. T. Price (1952), Part I. The diffraction theory of sea waves and the shelter afforded by breakwaters, *Philos. Trans. R. Soc. Lond.*, *244*, 236–253, doi:10.1098/rsta.1952.0003.

Roberts, H. H. (1974), Variability of reefs with regard to changes in wave power around an island, paper presented at the 2nd International Coral Reef Symposium, Brisbane, Australia.

Roberts, H. H., S. P. Murray, and J. N. Suhayda (1980), Physical process in a fringing reef system, *J. Mar. Res.*, *33*, 233–260.

Rogers, C. S. (1990), Responses of coral reefs and reef organisms to sedimentation. *Mar. Ecol.: Progr. Ser.*, *62*, 185–202, doi:10.3354/meps062185.

Rosman, J. H., and J. L. Hench (2011), A framework for understanding drag parameterizations for coral reefs, *J. Geophys. Res.*, *116*, C08025, doi:10.1029/2010JC006892.

Shinn, E. A. (1963), Spur and groove formation on the Florida reef tract, *J. Sediment. Petrol.*, *33*, 291–303.

Shinn, E. A., J. H. Hudson, R. B. Halley, and B. Lidz (1977), Topographic control and accumulation rates of some Holocene coral reefs: South Florida and Dry Tortugas, paper presented at the 3rd International Coral Reef Symposium, Miami, Fla.

Shinn, E. A., J. H. Hudson, D. M. Robbin, and B. Lidz (1981), Spurs and Grooves Revisited: Construction Versus Erosion Looe Key Reef, Florida, paper presented at the 4th International Coral Reef Symposium, Manila, Philippines

Sneh, A., and G. M. Friedman (1980), Spur and groove patterns on the reefs of the northern gulf of the Red Sea, *J. Sediment. Pet.*, *50*, 981–986.

Spalding, M. D., C. Ravilious, and E. P. Green (2001), *World Atlas of Coral Reefs*, prepared at the UNEP World Conserv. Monit. Cent., Univ. of Calif. Press, Berkeley, Calif.

Spydell, M., and F. Feddersen (2009), Lagrangian drifter dispersion in the surf zone: Directionally spread, normally incident waves, *J. Phys. Oceanogr.*, *39*, 809–830, doi:10.1175/2008JPO3892.1.

Storlazzi, C., and B. Jaffe (2008), The relative contribution of processes driving variability in flow, shear, and turbidity over a fringing coral reef: West Maui, Hawaii, *Estuarine Coastal Shelf Sci.*, *77*(4), 549–564, doi:10.1016/j.ecss.2007.10.012.

Storlazzi, C., J. Logan, and M. Field (2003), Quantitative morphology of a fringing reef tract from high-resolution laser bathymetry: Southern Molokai, Hawaii, *Geol. Soc. Am. Bull.*, *115*(11), 1344–1355, doi:10.1130/B25200.1.

Storlazzi, C., A. Ogston, M. Bothner, M. Field, and M. Presto (2004), Wave- and tidally-driven flow and sediment flux across a fringing coral reef: South-central Molokai, Hawaii, *Cont. Shelf Res.*, *24*(12), 1397–1419, doi:10.1016/j.csr.2004.02.010.

Storlazzi, C., E. Brown, M. Field, K. Rogers, and P. Jokiel (2005), A model for wave control on coral breakage and species distribution in the Hawaiian Islands, *Coral Reefs*, *24*, 43–55, doi:10.1007/s00338-004-0430-x.

Storlazzi, C., E. Elias, M. Field, and M. Presto (2011), Numerical modeling of the impact of sea-level rise on fringing coral reef hydrodynamics and sediment transport, *Coral Reefs*, *30*, 83–96. doi:10.1007/s00338-011-0723-9.

Svendsen, I. A. (2007), Introduction to nearshore hydrodynamics, in *Advanced Series on Ocean Engineering*, vol. *24*, World Scientific, Hackensack, N. J.

Symonds, G., K. Black, and I. Young (1995), Wave-driven flow over shallow reefs. *J. Geophys. Res.*, *100*(C2), 2639–2648, doi:10.1029/94JC02736.

Taebi, S., R. Lowe, C. Pattiaratchi, G. Ivey, G. Symonds, and R. Brinkman (2011), Nearshore circulation in a tropical fringing reef system, *J. Geophys. Res.*, *116*, C02016, doi:10.1029/2010JC006439.

Thomas, F., and M. Atkinson (1997), Ammonium uptake by coral reefs: Effects of water velocity and surface roughness on mass transfer, *Limnol. Oceanogr.*, *42*(1), 81–88, doi:10.4319/lo.1997.42.1.0081.

Weydert, P. (1979), Direction of growth of the spurs on an outer barrier reef tract—The example of the Grand Ré-cif of Tuléar (Madagascar), *Mar. Geol.*, *30*, 9–19.

Yahel, G., A. Post, K. Fabricius, D. Marie, D. Vaulot, and A. Genin (1998), Phytoplankton distribution and grazing near coral reefs, *Limnol. Oceanogr.*, *4*, 551–563, doi:10.4319/lo.1998.43.4.0551.